

## Radar and infrared observations of binary near-Earth Asteroid 2002 CE26

Michael K. Shepard<sup>a,\*</sup>, Jean-Luc Margot<sup>b</sup>, Christopher Magri<sup>c</sup>, Michael C. Nolan<sup>d</sup>,  
Joshua Schlieder<sup>e</sup>, Benjamin Estes<sup>e</sup>, Schelte J. Bus<sup>f</sup>, Eric L. Volquardsen<sup>g</sup>, Andrew S. Rivkin<sup>h</sup>,  
Lance A.M. Benner<sup>i</sup>, Jon D. Giorgini<sup>i</sup>, Steven J. Ostro<sup>i</sup>, Michael W. Busch<sup>j</sup>

<sup>a</sup> Department of Geography and Geosciences, Bloomsburg University of Pennsylvania, 400 E. Second St., Bloomsburg, PA 17815, USA

<sup>b</sup> Department of Astronomy, Cornell University, 304 Space Sciences Building, Ithaca, NY 14853, USA

<sup>c</sup> University of Maine at Farmington, Preble Hall, 173 High Street, Farmington, ME 04938, USA

<sup>d</sup> Arecibo Observatory, National Astronomy and Ionosphere Center, PR 00612, USA

<sup>e</sup> Department of Physics and Engineering Technology, Bloomsburg University, Bloomsburg, PA 17815, USA

<sup>f</sup> University of Hawaii, Hilo, HI 96720, USA

<sup>g</sup> Institute for Astronomy, 640 North A'ohoku Place, Hilo, HI 96720, USA

<sup>h</sup> Johns Hopkins Applied Physics Laboratory, Laurel, MD 20723, USA

<sup>i</sup> Jet Propulsion Laboratory, California Institute of Technology, Pasadena, CA 91109-8099, USA

<sup>j</sup> California Institute of Technology, Pasadena, CA 91109, USA

Received 17 February 2006; revised 6 April 2006

Available online 24 July 2006

### Abstract

We observed near-Earth Asteroid (NEA) 2002 CE26 in August and September 2004 using the Arecibo S-band (2380-MHz, 12.6-cm) radar and NASA's Infrared Telescope Facility (IRTF). Shape models obtained based on inversion of our delay-Doppler images show the asteroid to be  $3.5 \pm 0.4$  km in diameter and spheroidal; our corresponding nominal estimates of its visual and radar albedos are 0.07 and 0.24, respectively. Our IRTF spectrum shows the asteroid to be C-class with no evidence of hydration. Thermal models from the IRTF data provide a size and visual albedo consistent with the radar-derived estimate. We estimate the spin-pole to be within a few tens of degrees of  $\lambda = 317^\circ$ ,  $\beta = -20^\circ$ . Our radar observations reveal a secondary approximately 0.3 km in diameter, giving this binary one of the largest size differentials of any known NEA. The secondary is in a near-circular orbit with period  $15.6 \pm 0.1$  h and a semi-major axis of  $4.7 \pm 0.2$  km. Estimates of the binary orbital pole and secondary rotation rate are consistent with the secondary being in a spin-locked equatorial orbit. The orbit corresponds to a primary mass of  $M = 1.95 \pm 0.25 \times 10^{13}$  kg, leading to a primary bulk density of  $\rho = 0.9 + 0.5/-0.4$  g cm<sup>-3</sup>, one of the lowest values yet measured for a main-belt or near-Earth asteroid.

© 2006 Elsevier Inc. All rights reserved.

**Keywords:** Asteroids; Asteroids, composition; Asteroids, surfaces; Radar observations

### 1. Introduction

The Apollo near-Earth Asteroid (NEA) 2002 CE26 was discovered on 10 February 2002 by the Lincoln Laboratory (LINEAR) survey (MPEC 2002-C79). Pravec et al. (2006) reported a low amplitude lightcurve ( $\Delta m < 0.1$  mag) with a synodic period  $P = 3.2930 \pm 0.0004$  h. The relatively rapid rotation and low lightcurve amplitude of 2002 CE26 were noted to be

similar to previously discovered binary systems, but no eclipse events were detected (Pravec et al., 2006). Subsequent phase angle analysis revealed it to have an absolute magnitude  $H = 15.8 + 0.2/-0.3$  and a steep phase parameter  $G = -0.25 \pm 0.05$  (Pravec et al., 2006). Table 1 summarizes these previously known physical properties.

In this paper, we describe continuous wave (CW, Doppler-only) and delay-Doppler radar observations acquired over four days at the Arecibo Observatory and near-infrared (NIR) observations from the Infrared Telescope Facility (IRTF). In the remainder of this section, we summarize the optical and radar

\* Corresponding author. Fax: +1 570 389 3028.

E-mail address: [mshepard@bloomu.edu](mailto:mshepard@bloomu.edu) (M.K. Shepard).

Table 1  
Physical properties

Property	Value
$H$ (mag)	$15.8 + 0.2/-0.3$
$G$ (mag/deg)	$-0.25 \pm 0.05$
$P$ (h) (synodic)	$3.2930 \pm 0.0004$
$\Delta m$ (mag)	$\sim 0.06$

Note.  $H$  is absolute magnitude.  $G$  is phase parameter.  $P$  is rotation period.  $\Delta m$  is the lightcurve amplitude. All data are from Pravec et al. (2006).

model parameters, equations, and uncertainties that we use throughout this paper.

To place constraints on an asteroid's diameter, we use the relationship between visual albedo ( $p_v$ ), effective diameter (the diameter of a sphere with the same projected area as the asteroid,  $D_{\text{eff}}$ , in km) and absolute magnitude ( $H$ ) given by Fowler and Chillemi (1992)

$$\log p_v = 6.247 - 2 \log D_{\text{eff}} - 0.4H. \quad (1)$$

Our radar observational, reduction, and analysis techniques are similar to those described by Mitchell et al. (1996) and Ostro et al. (2002, 2005a). Each observing cycle or "run" consisted of transmission of a circularly polarized, 2380-MHz (12.6 cm) signal for the round-trip light travel time to the target, followed by reception of echoes for a comparable duration in the opposite (OC) and same (SC) senses of polarization as transmitted. We operated in three modes: continuous wave (CW), ranging, and delay-Doppler imaging. Our reduction of raw echo power spectra included background removal, calibration, and the formation of sums of spectra weighted according to system performance (gain, system temperature, and transmitted power).

The radar albedo,  $\hat{\sigma}_{\text{OC}}$ , of an asteroid is the ratio of its OC radar cross section ( $\sigma_{\text{OC}}$ ) to its cross-sectional area,

$$\hat{\sigma}_{\text{OC}} = \frac{4\sigma_{\text{OC}}}{\pi D_{\text{eff}}^2}. \quad (2)$$

Published asteroid radar albedos range from a low of 0.04 for the G-class main-belt asteroid (MBA) 1 Ceres (Mitchell et al., 1996) and NEA 1566 Icarus (Mahapatra et al., 1999) to a maximum of 0.6 for the M-class object 216 Kleopatra (Ostro et al., 2000). See Benner (2006) for a summary of asteroid radar properties.

The instantaneous bandwidth  $B$  of a radar echo is related to the radar wavelength  $\lambda$ , the target's physical properties and its orientation by

$$B(\phi) = \frac{4\pi D(\phi)}{\lambda P} \cos \delta, \quad (3)$$

where  $D(\phi)$  is the asteroid's plane-of-sky extent normal to the apparent spin vector at rotation phase  $\phi$ ,  $P$  is the apparent rotation period, and  $\delta$  is the angle between the radar line-of-sight and the object's apparent equator. With  $D$  in km,  $B$  in Hz,  $P$  in h, and  $\lambda$  of 0.126 m, Eq. (2) can be rewritten

$$D(\phi) = \frac{PB(\phi)}{27.7 \cos \delta}. \quad (4)$$

We estimate the minimum bandwidth and the corresponding lower bound on the maximum pole-on breadth,  $D_{\text{max}}$ , using

Eq. (4). Our experience with other asteroids suggests that a reasonable estimate of the bandwidth can be made from the points where the echo power spectrum first drops to two standard deviations of the background noise (referred to as the two-sigma-crossing threshold).

Uncertainties in our estimates of radar cross-section (obtained by integrating the spectra) are typically  $\pm 25\%$  and are based on prior experience with systematic uncertainties in pointing and calibration. Because systematic uncertainties are nearly the same for both polarizations, uncertainties in the polarization ratio,  $\mu_c (= \sigma_{\text{sc}}/\sigma_{\text{oc}})$ , are due primarily to receiver noise.

Our quoted uncertainties for other measured parameters (e.g., polarization ratio) are one standard-deviation assuming Gaussian statistics. The uncertainties quoted for derived parameters (size, radar albedo, bulk density, etc.) are conservative and, unless specified otherwise, give the *full range* of possible values by folding in all other known sources of error.

## 2. Observations and analysis

### 2.1. Near infrared spectroscopy

We acquired near-infrared (NIR) spectral observations at the 3.0-m NASA Infrared Telescope Facility (IRTF) using the Spex instrument (Rayner et al., 2003). The first observations were made in prism mode (0.8–2.5  $\mu\text{m}$ ,  $0.8'' \times 15''$  slit,  $R \sim 100$ ) on 23 August 2004 between 11:20 and 12:15 UT when 2002 CE26 was at a solar phase angle of  $40^\circ$ . A total of 12 observations of 2 min integration each were acquired, processed using the IRAF software package (<http://iraf.noao.edu>), corrected for telluric water using the ATRAN model (Lord, 1992), ratioed to the solar analog star SAO 231044, and summed (Fig. 1).

A second set of spectra were acquired in LXD mode (2.2–4.2  $\mu\text{m}$ ,  $0.8'' \times 15''$  slit,  $R \sim 940$ ) on 29 August 2004 between 10:30 and 14:25 UT when 2002 CE26 was at a solar phase angle of  $28^\circ$ . A total of 60 observations of 15 s integration each were acquired, processed using the SpeXtool (Cushing et al., 2004), corrected for telluric water using the ATRAN model, ratioed to solar analog stars (HD 377 and HD 217577), and summed (Fig. 2).

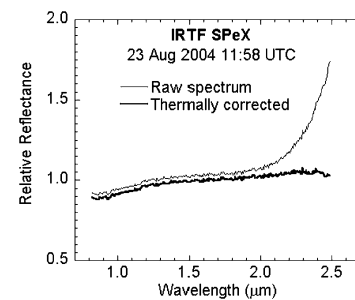


Fig. 1. Near-infrared spectrum (prism mode, 0.4–2.5  $\mu\text{m}$ ) acquired on 23 August 2004 11:58 UTC. Note the large increase (thermal component) in the raw spectrum at wavelengths greater than 2.2  $\mu\text{m}$ . The thermally corrected spectrum is shown as the bold line and is most consistent with a C-classification. Uncertainties are on the order of the jitter observed in each spectrum.

Table 2  
Radar observations (2004)

Date	RA (°)	Dec. (°)	$\lambda$ (°)	$\beta$ (°)	Dist. (AU)	Runs	Setup mode	UT receive start–stop
27 August	351	27	4	28	0.180	2	cw	04:15–04:29
27 August	351	27	4	28	0.180	2	ranging	04:30–04:43
27 August	351	27	4	28	0.180	2	cw	04:45–04:58
27 August	351	27	4	28	0.180	16	1.0 $\mu\text{s}/2$ spb	05:05–06:41
30 August	355	17	2	18	0.143	23	1.0 $\mu\text{s}/2$ spb	05:00–06:49
31 August	356	12	1	13	0.132	22	1.0 $\mu\text{s}/2$ spb	04:30–06:06
2 September	359	1	0	1	0.114	2	cw	05:04–05:13
2 September	359	1	0	1	0.114	7	0.3 $\mu\text{s}/3$ spb	05:17–05:45

Notes. RA, DEC are J2000 at center of observation window.  $\lambda$  and  $\beta$  are ecliptic longitude and latitude, respectively. Runs is the number of transmit–receive cycles. Setup mode is continuous wave (cw), ranging (4 and 4.5  $\mu\text{s}$  band), or delay–Doppler imaging with the baud rate/samples per baud (spb) shown. Multiple samples per baud result in correlated range pixels. Start–stop gives the beginning and end of a series of runs (in UTC).

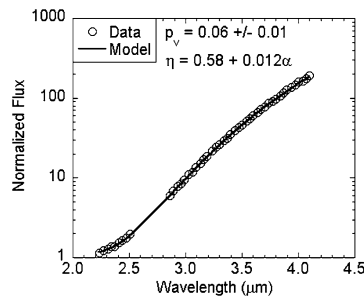


Fig. 2. Near-infrared spectrum (LXD mode, 2.2–4.4  $\mu\text{m}$ ) acquired on 29 August 2004. Normalized flux is (emitted + reflected)/reflected flux. Shown are data (circles) and best NEATM fit (line) giving a visual albedo of  $0.06 \pm 0.01$ .

For thermal modeling, spectra were rebinned into increments of 0.01  $\mu\text{m}$  and fit with the near-Earth Asteroid Thermal Model (NEATM; Harris, 1998). The NEATM was developed to deal with the high phase angles commonly encountered in observations of NEAs and to allow flexibility with the ‘beaming parameter’  $\eta$ , a measure of an asteroid’s tendency to direct thermal energy in a backscattering direction (Harris and Lagerros, 2002). We created a number of thermal models with varying albedos and beaming parameters and adopted the model with the lowest  $\chi^2$  residual. Uncertainties were determined by noting the model parameter values at which deviations from the observed spectrum exceeded one standard deviation ( $\sim 2\%$ ).

Our prism mode (0.8–2.5  $\mu\text{m}$ ) spectrum is featureless and red-sloped and is most consistent with a C-classification. This spectrum is notable for its large thermal component ( $>2.2$   $\mu\text{m}$ ) suggesting a pole orientation toward the Sun, low thermal inertia, or both, and is consistent with our LXD mode spectrum (2.2–4.2  $\mu\text{m}$ ). Near-Earth objects are warm enough that their thermal flux is easily detectable at the longest wavelengths in the prism-mode spectra as well as in the longer wavelength LXD mode. Rivkin et al. (2005) showed that near-IR spectra can be used in these cases to constrain the albedos of target asteroids, given reasonable assumptions. Because 2002 CE26 was observed in both modes, independent modeling constrains 2002 CE26’s visual albedo to be  $p_v = 0.06 \pm 0.01$  (see Fig. 2) with a beaming parameter  $\eta = 0.58 + 0.012\alpha$ , where  $\alpha$  is the solar phase angle in degrees. Given 2002 CE26’s absolute magnitude (Table 1), the visual albedo corresponds to an effective diameter of  $3.8 + 0.9/-0.5$  km, where most of the uncertainty is due

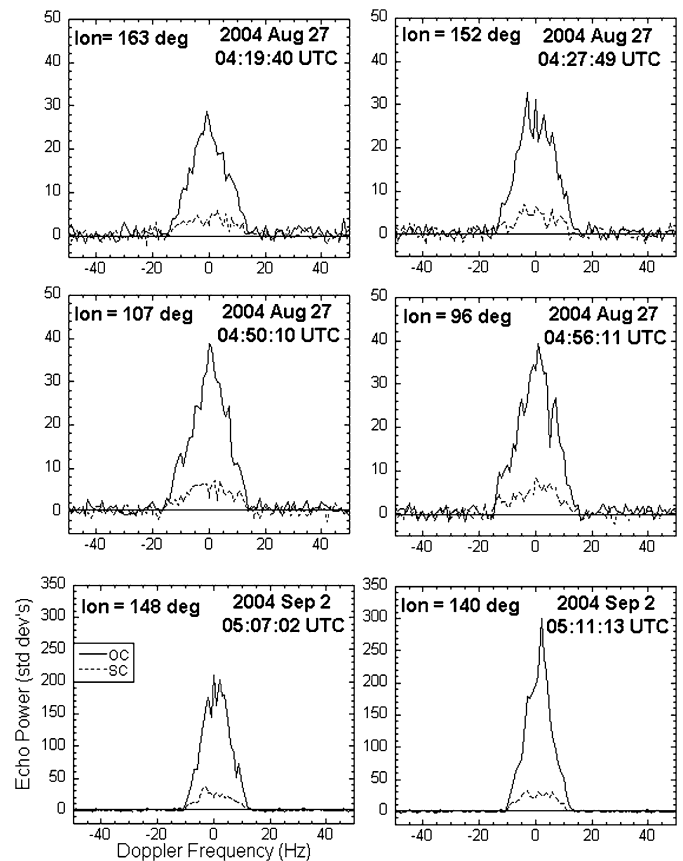


Fig. 3. Continuous wave (CW) observations. Date, time, and subradar longitude (using final shape model reference) in degrees are shown. Frequency resolution is 1 Hz.

to the large uncertainty in the absolute magnitude. We find no evidence of a 3  $\mu\text{m}$  water of hydration feature at the 5% level of detection.

## 2.2. Radar

### 2.2.1. Observations

We observed 2002 CE26 on four days at Arecibo between 27 August and 2 September 2004. We acquired a total of six CW observations of 2002 CE26; four observations were acquired on 27 August and two on 2 September 2004 (Fig. 3, Table 2). After initial CW detection on 27 August, we changed observing

Table 3  
Orbit

Quantity	Value	Uncertainty
Epoch 2453161.50000 = 2004 June 5.00000		
Eccentricity	0.5591774598284251	$\pm 0.0000000144$
Perihelion distance	0.9843796149279309	$\pm 0.0000000416$ AU
Perihelion date	2453292.3070620272	$\pm 0.0000054414$ d (2004 October 13.80706)
Long. Asc. node	162.04406760698230	$\pm 0.0000008279^\circ$
Arg. perihelion	227.93907461928240	$\pm 0.0000082413^\circ$
Inclination	47.35768837086655	$\pm 0.0000040166^\circ$
Semimajor axis	2.233051909153274	$\pm 0.0000001004$ AU
Period	1218.839877804041	$\pm 0.00008217$ d (3.33694324809652 yr)
Mean anomaly	321.36445550612420	$\pm 0.0000026268^\circ$

Note. 2002 CE26 heliocentric J2000 orbital elements (OSOD #64). Uncertainties are one std. deviation.

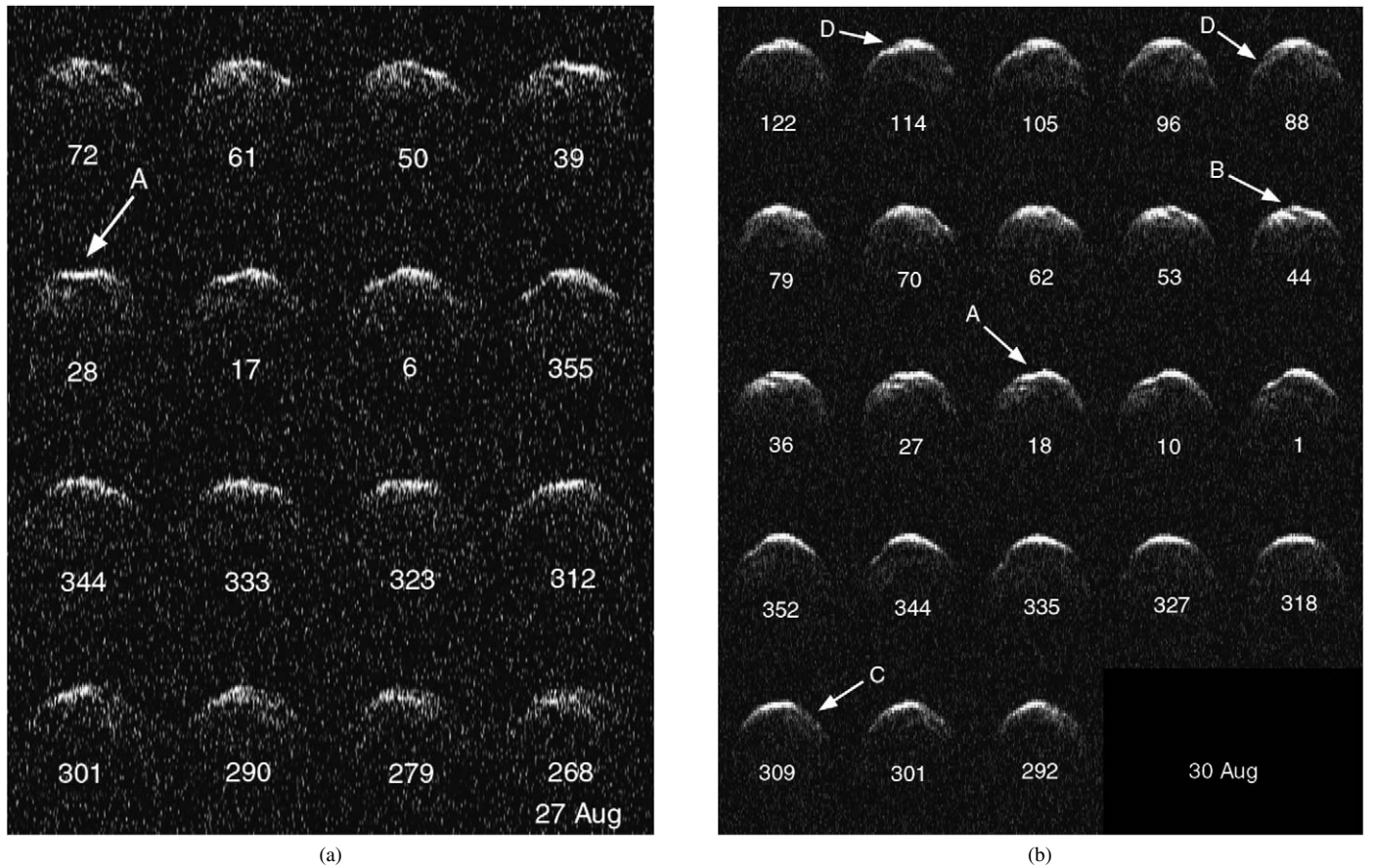
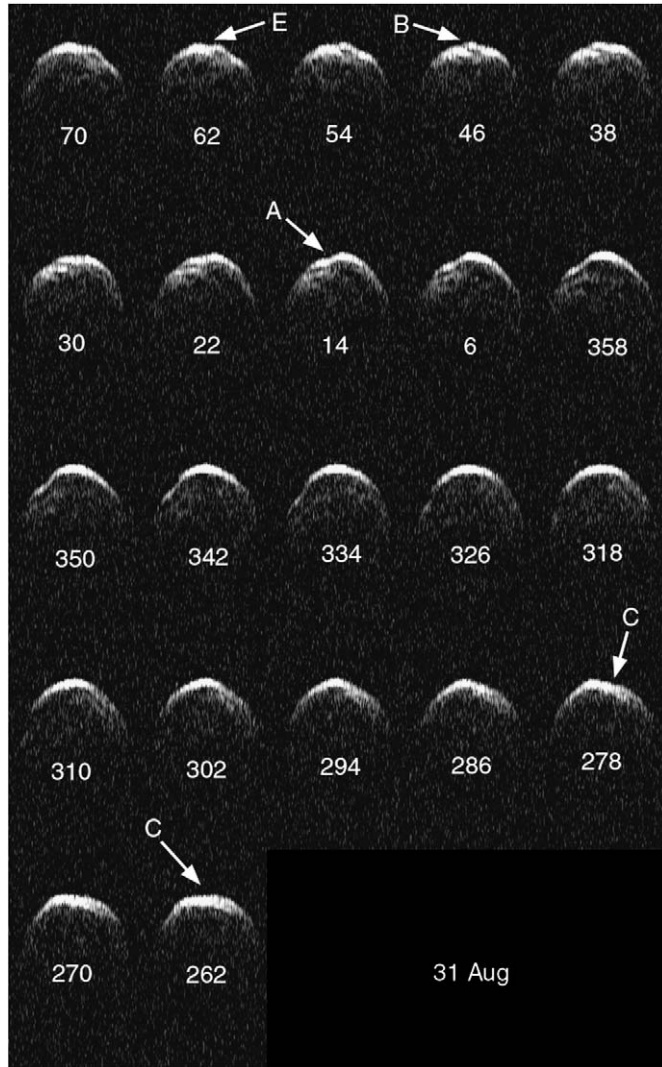


Fig. 4. Mosaics of all images acquired (a) 27 August, (b) 30 August, (c) 31 August, and (d) 2 September 2004. In all images, Doppler frequency increases from left to right and range from top to bottom. August images have a frequency resolution of 0.24 Hz and range resolution of 75 m/pixel, but have been resampled to a range resolution of 25 m/pixel for ease of comparison. The size of an August individual image is 34 Hz by 4500 m. September images have a frequency resolution of 0.10 Hz and range resolution of 15 m/pixel. The individual September images are 26 Hz by 2100 m. Longitude of subradar point (with respect to final shape model) is indicated. Arrows and letters point to features discussed in text.

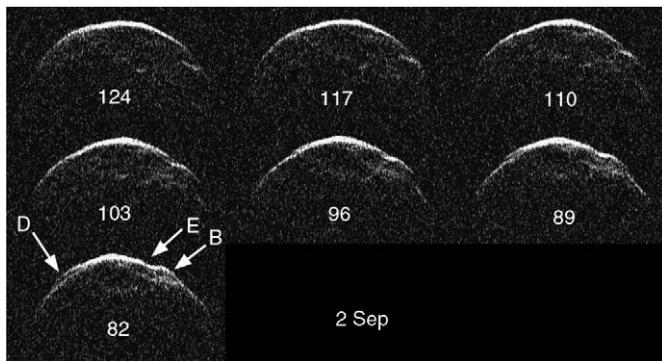
modes and acquired two ranging runs with time-delay resolutions (“bauds”) of 4 and 4.5  $\mu$ s (600 and 675 m) to improve the orbital ephemeris using JPL’s On-Site Orbit Determination program (OSOD). A range correction of 886  $\mu$ s was added to generate Solution 49 which was used throughout the rest of the experiment. A more detailed analysis of the images subsequent to the experiment revised this correction to 889.48  $\mu$ s. The most recent orbit (Solution 64) is given in Table 3.

We acquired delay-Doppler images on each day with effective resolutions of 15–75 m/pixel in range (Fig. 4, Table 2). Because we over-sampled our received signals on all days, adjacent range pixels are positively correlated.

We reference positions on 2002 CE26 to subradar longitudes and latitudes determined with our shape model (Section 2.2.3). In this right-handed system, 0° longitude (lon) is along the major axis of the model (+x-axis), the +y-axis is perpendicular



(c)



(d)

Fig. 4. (continued)

at lon  $90^\circ$ , and the  $z$ -axis is perpendicular to  $x$ - and  $y$ -axes and equivalent to the rotation pole.

We observed  $\sim 270^\circ$  of rotation on 27 August,  $180^\circ$  of rotation on 30 and 31 August, and  $75^\circ$  on 2 September. The subradar longitudes ranged from  $260^\circ$  to  $160^\circ$ . In all cases, the transmit–receive cycles were 4–6 min in duration resulting in a rotational smear of  $\leq 6^\circ$ .

Table 4  
Secondary observations

MJD	Date UTC	RNG (km)	DOP (Hz)
53244.214	27 August 05:08:20	−2.03	7.16
53244.247	27 August 05:56:13	−3.30	5.49
53244.264	27 August 06:20:05	−3.71	4.18
53244.268	27 August 06:26:03	−4.05	4.06
53247.210	30 August 05:02:32	3.80	−2.38
53247.213	30 August 05:07:20	3.90	−2.14
53247.217	30 August 05:12:04	3.90	−2.02
53247.220	30 August 05:16:52	4.05	−1.90
53247.223	30 August 05:21:36	4.13	−1.42
53247.227	30 August 05:26:24	4.05	−1.30
53247.230	30 August 05:31:08	4.05	−1.07
53247.233	30 August 05:35:56	4.13	−0.71
53247.243	30 August 05:50:10	4.05	−0.12
53247.246	30 August 05:54:54	4.13	0.25
53247.250	30 August 05:59:38	4.05	0.37
53247.253	30 August 06:04:22	3.98	0.48
53247.256	30 August 06:09:06	3.98	0.72
53247.260	30 August 06:13:50	3.98	0.96
53247.266	30 August 06:23:18	3.98	1.44
53247.269	30 August 06:28:02	3.90	1.68
53247.273	30 August 06:32:46	3.83	1.92
53247.276	30 August 06:37:30	3.90	2.24
53247.279	30 August 06:42:14	3.83	2.39
53247.283	30 August 06:46:58	3.83	2.63
53248.189	31 August 04:32:06	−3.90	2.03
53248.192	31 August 04:36:30	−3.90	1.86
53248.195	31 August 04:40:54	−3.90	1.62
53248.198	31 August 04:45:18	−4.09	1.38
53248.201	31 August 04:49:42	−4.05	1.20
53248.204	31 August 04:54:06	−4.05	0.96
53248.207	31 August 04:58:30	−4.05	0.78
53248.210	31 August 05:02:54	−4.09	0.54
53248.213	31 August 05:07:18	−4.09	0.37
53248.216	31 August 05:11:42	−4.05	0.13
53248.220	31 August 05:16:06	−4.05	−0.05
53248.223	31 August 05:20:30	−4.05	−0.29
53248.226	31 August 05:24:54	−4.05	−0.47
53248.229	31 August 05:29:18	−4.05	−0.65
53248.232	31 August 05:33:42	−4.09	−0.89
53248.235	31 August 05:38:06	−4.05	−1.07
53248.238	31 August 05:42:30	−3.98	−1.30
53248.241	31 August 05:46:54	−3.94	−1.54
53248.244	31 August 05:51:18	−3.98	−1.78
53248.247	31 August 05:55:42	−3.90	−1.90
53248.250	31 August 06:00:06	−3.94	−2.08
53248.253	31 August 06:04:30	−3.83	−2.26
53250.222	2 September 05:19:44	−2.82	−3.39
53250.225	2 September 05:23:33	−2.75	−3.59
53250.227	2 September 05:27:23	−2.67	−3.69
53250.230	2 September 05:31:13	−2.61	−3.79
53250.233	2 September 05:35:03	−2.51	−3.89
53250.235	2 September 05:38:53	−2.43	−3.99
53250.238	2 September 05:42:43	−2.33	−4.09

*Notes.* MJD is the modified Julian date at the starting time of data reception. RNG is the distance between secondary's center-of-mass (COM) and the primary's COM. Negative distances indicate the secondary is closer to the observer than the primary, positive distances indicate the secondary is farther from the observer. DOP is the difference of secondary Doppler COM from primary COM. Uncertainties are  $\pm 0.30$  km in range and  $\pm 0.48$  Hz in Doppler for 27 August,  $\pm 0.15$  km in range and  $\pm 0.24$  Hz for 30 and 31 August, and  $\pm 0.1$  km in range and  $\pm 0.20$  Hz for 2 September.

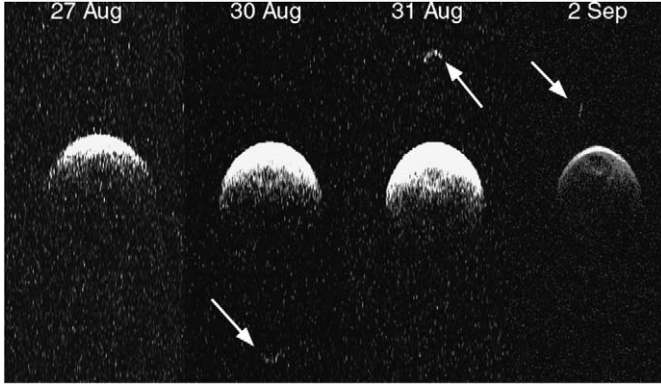


Fig. 5. Composite of daily weighted sums of images enhanced to show the secondary. All images have been resampled to a frequency resolution of 0.24 Hz and range resolution of 25 m/pixel. The size of each daily frame is 42 Hz by 10 km. Doppler frequency increases from left to right and range increases from top to bottom in all images.

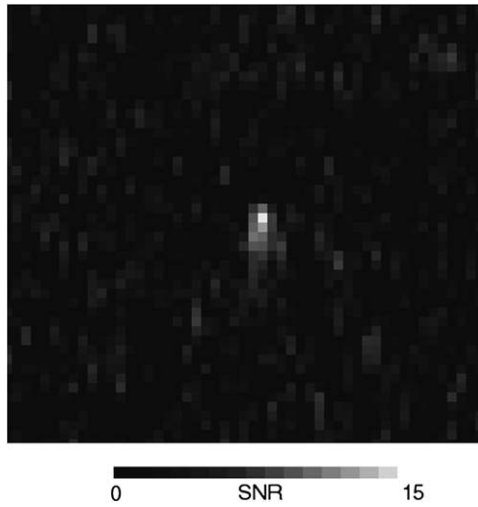


Fig. 6. Delay-Doppler image showing the secondary on 2 September 05:23:33 UTC. Range increases from top to bottom and Doppler frequency increases from left to right. Frequency and range resolutions are 0.10 Hz and 15 m, respectively. Image has been stretched so that  $\text{SNR} \leq 1.0$  are black and  $\text{SNR} \geq 15$  are white.

### 2.2.2. Satellite

Our delay-Doppler images revealed a small secondary (Table 4, Fig. 5; Shepard et al., 2004). On 30 August, the secondary passed through superior geocentric conjunction at 05:51 UT, and on 31 August, it passed through inferior conjunction at 05:15 UT. Based on these observations, we measured an apparent orbital range extent of  $8.2 \pm 0.2$  km, providing a lower bound on its semi-major axis  $a_{\min} = 4.0$  km. If the orbit is inclined significantly with respect to our radar line of sight on these dates, the semi-major axis will be larger. Observations on 2 September indicate that the secondary is 0.7 to 0.9  $\mu\text{s}$  (105 to 135 m) in apparent delay-depth and  $0.4 \pm 0.1$  Hz in Doppler frequency (Fig. 6), leading to a diameter estimate of  $0.3 \pm 0.1$  km and (folding in all uncertainties) constraining the rotation period to be  $\leq 37$  h. A summary of secondary properties is given in Table 5. We refine the orbital elements below, using a shape model for the primary (Section 2.2.4).

Table 5  
Secondary properties

Orbital period (h)	$15.6 \pm 0.1$
Orbital inclination ( $^\circ$ )	0–45 (see Fig. 10)
Rotation period (h)	$\leq 37$ ( $15 + 11/-7$ )
Eccentricity	$0.00 \pm 0.02$
Semimajor axis (km)	$4.7 \pm 0.2$
$D_{\text{eff}}$ (km)	$0.3 \pm 0.1$

Note. There are two estimates of rotation period: the first assumes no specific secondary spin pole and the second (in parentheses) assumes a secondary spin pole parallel to the primary spin pole.

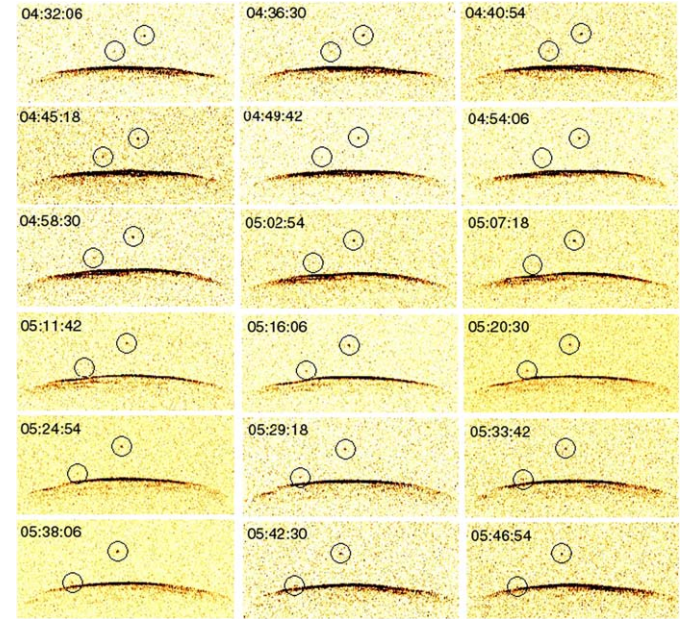


Fig. 7. Composite of images on 31 August showing features consistent with a possible tertiary satellite. Times are in UTC. Circles are centered on secondary (near top) and feature (between secondary and primary). The feature is not evident in images at 05:07:18 or 05:11:42. It appears to merge with the primary at 05:46:54 and is not evident afterward. Image resolution is 0.12 Hz in Doppler and 75 m in delay. Each frame is 27 Hz by 7600 m. Doppler frequency increases from left to right and range from top to bottom in all images.

On images acquired on 31 August, we observe a uniformly moving feature that could be interpreted as a tertiary component (Fig. 7), considerably weaker in SNR than the secondary and moving more rapidly than it in both time-delay and Doppler frequency. Given our limited observation span, it is not possible to determine an orbit for the candidate tertiary. However, using the method described by Margot et al. (2002), we found numerous solutions with low  $\chi^2$  residuals ( $< 1.0$ ) which were consistent with our estimate of the primary mass (see Section 2.2.5).

The ‘tertiary’ does not appear to be due to random noise. It has an  $\text{SNR} \geq 3$  in 14 out of 17 observations. Furthermore, the feature shows Doppler spreading of four adjacent frequency bins (in the same range gate) with  $\text{SNR} \geq 4$  in the 05:20:30 image (0.06 Hz/bin, Fig. 8). The image just prior (05:16:06) shows three adjacent frequency bins with  $\text{SNR} \geq 3.0$ . Excluding the primary and secondary, we find that there are no other features within any of the other 17 images where four adjacent

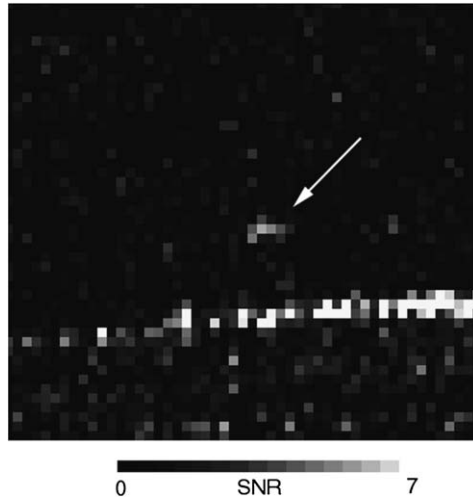


Fig. 8. Arrow shows purported tertiary on 31 August 05:20:30 UT. Range increases from top to bottom and Doppler frequency increases from left to right. Frequency and range resolutions are 0.06 Hz and 75 m, respectively. Images have been stretched so that  $\text{SNR} \leq 1.0$  are black and  $\text{SNR} \geq 7$  are white. The leading edge of the primary is visible along the bottom half of the frame.

Table 6  
Disc-integrated radar properties from CW data

Date	UT time	SNR	BW (Hz)	$\mu_c$	$\sigma_{oc}$ (km <sup>2</sup> )	Lon. (°)
27 August	04:19:40	84	27.1	0.23	2.09	163
27 August	04:27:49	97	26.5	0.22	2.04	152
27 August	04:50:10	112	29.2	0.24	2.10	107
27 August	04:56:11	116	28.2	0.23	2.23	96
2 September	05:07:21	572	24.2	0.19	3.26	148
2 September	05:11:13	668	24.3	0.19	3.49	140

Note. SNR is signal-to-noise of the optimally filtered observation. BW is the bandwidth of the signal estimated as the point where the signal drops to two-standard-deviations of noise from observations with frequency resolution 1.0 Hz. Uncertainties  $\pm 1$  Hz.  $\mu_c$  is the polarization ratio. Uncertainties are  $\pm 0.01$ .  $\sigma_{oc}$  is the radar cross-section in km<sup>2</sup>. Uncertainties are  $\pm 25\%$ . Lon. is the sub-radar longitude using our shape model as a reference.

bins show  $\text{SNR} \geq 4$ , and three adjacent bins of  $\text{SNR} \geq 3.0$  occur only once in any other image.

It is puzzling that we do not see the feature on any other day. The SNR was weaker on 27 and 30 August, but significantly stronger on 2 September. Is it masked by the primary on that date? Or are the observations on 31 August simply due to a spurious but unknown cause? Without corroborating observations on another day, the evidence for a tertiary remains tantalizing but inconclusive.

### 2.2.3. Primary size, shape, and pole

Our bandwidth estimates for the weighted (by SNR) daily sums of 27 August and 2 September are 29.1 and 24.5 Hz, respectively (Table 6). The larger bandwidth places a lower bound [Eq. (4)] of  $3.4 \text{ km} / \cos \delta$  on the maximum diameter. We examined each delay-Doppler image and observed only minor variations in bandwidth between individual runs during a given day, consistent with the low amplitude of the lightcurve, and suggesting an ellipsoid approximation with  $a/b \sim 1$ . We also summed each set of daily images and measured their maximum

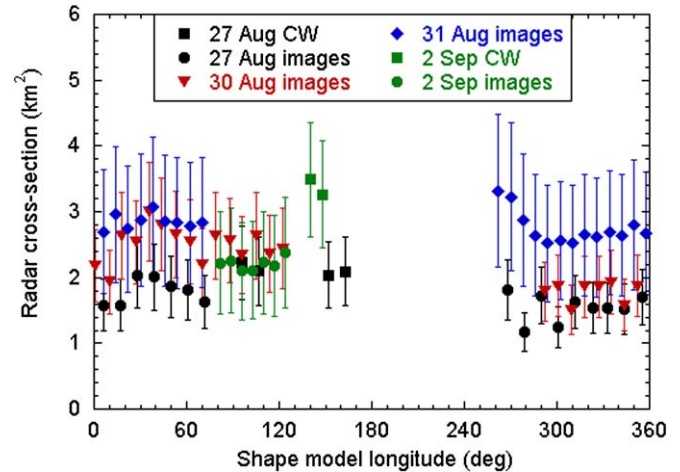


Fig. 9. Radar cross-section estimated from CW and delay-Doppler images as a function of shape model longitude. Uncertainties are  $\pm 25\%$  for all data except 2 September images which are  $\pm 35\%$  because those images were not match-filtered. Our best estimate of the mean cross-section is  $2.3 \pm 1.0 \text{ km}^2$ .

delay-depth. Assuming this to be half the diameter (strictly appropriate only for a spheroid), we obtained a similar and independent estimate of  $3.5 \pm 0.2 \text{ km}$  for 2002 CE26's maximum diameter, leading us to conclude that our subradar latitude was near-equatorial around 27 August.

From the CW observations, we measured the daily radar cross-sections to be  $2.2 \pm 0.5 \text{ km}^2$  on 27 August and  $3.4 \pm 0.8 \text{ km}^2$  on 2 September. These observations were acquired at about the same subradar longitudes, yet are consistent only at the extremes of their uncertainty estimates. To assess the reality of the variations, we calibrated our 68 delay-Doppler images. Fig. 9 shows a plot of radar cross-section (km<sup>2</sup>) versus longitude for all CW and delay-Doppler image cross-sections. While there is some evidence for a general increase in radar cross-section with date—possibly linked to a change in subradar latitude—these variations may also be due to systematic uncertainties in pointing or calibration. It is also possible that the larger than expected cross-section on 2 September is due to structurally-caused specular glints, as suggested by the large spike observed in the second CW run on that date (see Fig. 3). We therefore take the mean of all cross-section measurements as our estimate,  $\sigma_{oc} = 2.3 \pm 1.0 \text{ km}^2$ . 2002 CE26's polarization ratio for the unweighted averaged sum of all CW observations is  $0.21 \pm 0.02$ , which is in the lower half of observed NEAs but not otherwise unusual (Benner, 2006).

Our delay-Doppler images show evidence of numerous large features (depressions, knobs, and flat areas) which are observed on multiple days (Fig. 4). We refer to these as features A through E. Tracking these features confirms the rotation period published by Pravec et al. (2006). Feature A occurs at longitude (lon)  $\sim 30^\circ$  and appears to be a circular depression or indentation with an associated bump or knob (feature B) at lon  $\sim 45^\circ$ . Feature C appears to be a large flat facet centered at longitude  $\sim 260^\circ$ . Feature D appears to be a depression at longitude  $\sim 130^\circ$  and is most evident on 2 September on the negative Doppler edge of frames at longitude  $82^\circ$  and  $89^\circ$ . Feature E appears to be another depression located at longitude  $\sim 60^\circ$  and

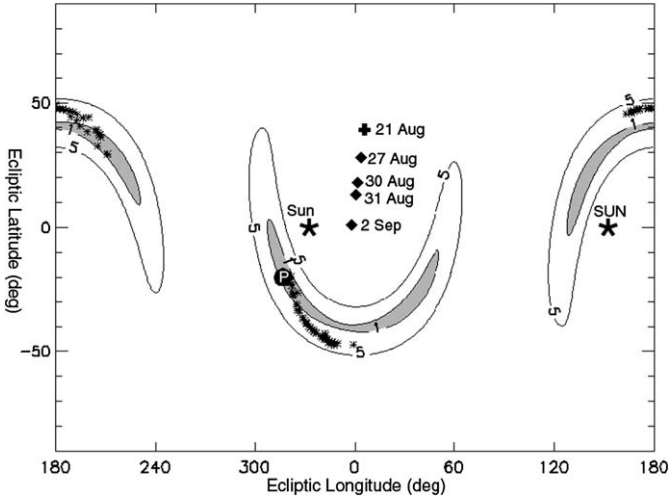


Fig. 10.  $\chi^2$  contours for ellipsoid models with  $D_{\max} = 3.6$  km and all possible primary spin poles. Gray regions indicate spin-pole locations with  $\chi^2 \leq 1$ . The diamonds show the center position of 2002 CE26 at the midpoint of our observations on each day. The cross shows its position at the lightcurve epoch. The larger stars show the position of the Sun on 23 August ('SUN')—the time of our IRTF prism mode observation—and its mirror position ('Sun'). The dark circle and 'P' shows our adopted primary spin-pole and the smaller asterisks show the locations of our best binary orbital poles (model  $\chi^2 < 0.5$ ).

is first evident on 31 August and later on 2 September. It is not readily visible on the 30 August images at the same longitude, suggesting it to be at higher latitudes. There is evidence of additional large scale structures in the 2 September images away from the leading edge but these are not visible on the other days.

2002 CE26 moved  $\sim 30^\circ$  across the sky during our observations, allowing us to use observed variations in bandwidths to constrain its rotation pole. We used the bandwidths of the daily weighted sums of CW and, in addition, we created daily sums of images and estimated the bandwidths of these by collapsing them in delay and locating their 2-sigma crossing points. For a range of diameters, we calculated the expected CW bandwidth for every possible pole direction; when compared with our observed bandwidths, this leads to a  $\chi^2$  estimate for each possible pole. Fig. 10 shows a contour map of  $\chi^2$  for an ellipsoid of  $D_{\max} = 3.6$  km. For maximum diameters of 3.4–4.0 km, the lowest  $\chi^2$  regions are typically within  $20^\circ$  of those indicated. Also shown are the locations of 2002 CE26 during our observations (diamonds) and at the Pravec et al. (2006) lightcurve epoch (cross), and the position of sun and its mirror (star symbols) at the time of our prism-mode IRTF spectrum (August 23). Restricting ourselves to regions where  $\chi^2 \leq 1$ , two arcuate regions, shaded gray in Fig. 10, define potential poles.

To model the shape and size of 2002 CE26, we used software and methods outlined by Hudson (1993) and most recently described by Ostro et al. (2005a) and Busch et al. (2006). In short, we began by using ellipsoid models to synthesize delay-Doppler images, CW echoes, and lightcurves that were compared to the actual data. We incorporated all of the delay-Doppler images and CW data. We opted to compare our synthetic lightcurve to the model lightcurve reported by Pravec et al. (2006), sampled every  $3.6^\circ$  (100 points), instead of the raw lightcurve data. Because the lightcurve is well behaved and low-

Table 7  
Properties of the shape model

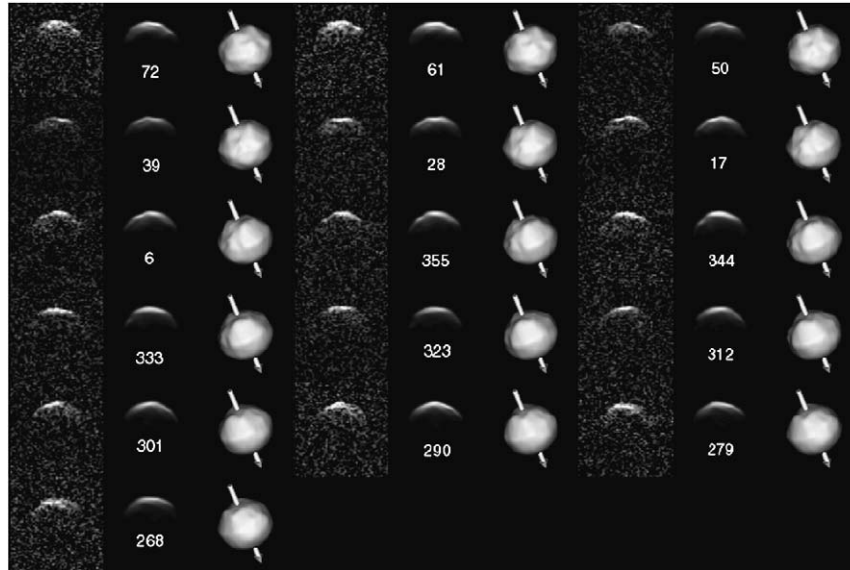
Maximum dimensions	
x-axis	$3.65 \text{ km} \pm 10\%$
y-axis	$3.65 \text{ km} \pm 10\%$
z-axis	$3.26 \text{ km} \pm 10\%$
Pole ( $\lambda, \beta$ )	$317^\circ \pm 10, -20 \pm 15^\circ$
Rotation period (h)	$3.2931 \pm 0.0003$
Surface area ( $\text{km}^2$ )	$38.1 \pm 20\%$
Volume ( $\text{km}^3$ )	$21.7 \pm 30\%$
$D_{\text{eff}}$ (km)	$3.46 \pm 10\%$
DEEVE (km)	$3.60 \times 3.58 \times 3.21 \pm 10\%$

Note.  $D_{\text{eff}}$  is the diameter of a sphere with the model's volume. DEEVE is dimensions of the dynamically equivalent equal-volume ellipsoid, a homogeneous ellipsoid having the same moment-of-inertia ratios and volume as model.

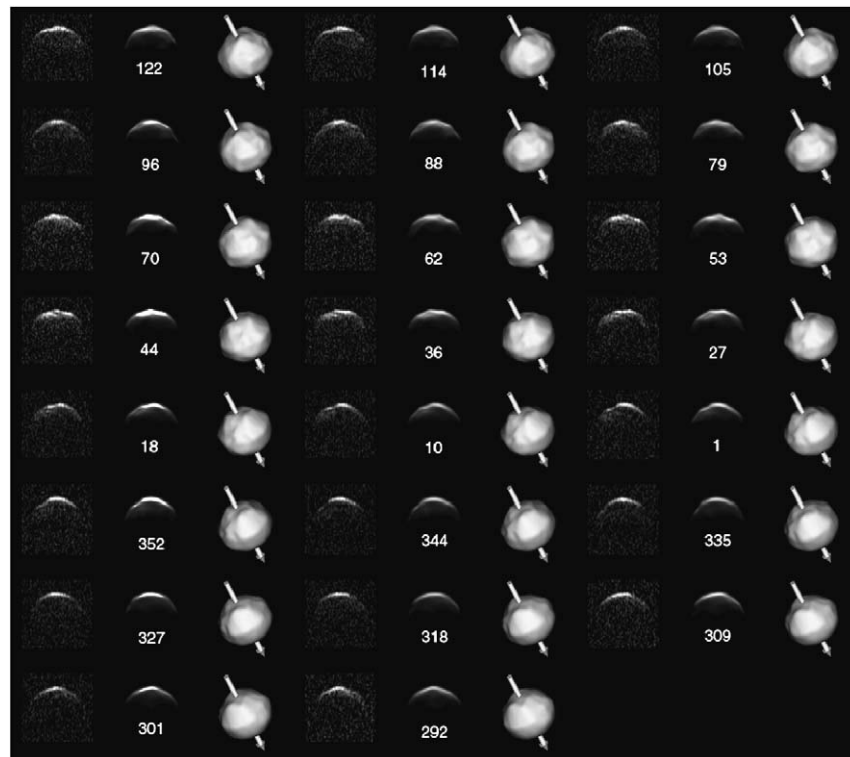
amplitude and the raw data are scattered within  $\sim 0.02$  magnitudes of their model fit, we expected little or no degradation in our final shape model. This also saved enormous computing resources and allowed us to explore parameter space more efficiently.

We started the shape modeling process with a large range of ellipsoid models that varied in size, axis ratio, scattering law, and rotation pole. The rotation rate was treated as a free parameter and allowed to float. We conducted a broad grid search for the pole and found the least-squares minimum to be consistent with our contour map (Fig. 10). The better ellipsoid models (i.e., those with the lowest shape model  $\chi^2$  residuals) were converted into vertex models; in our case, we utilized models with 1148 vertices, giving 'facets' that are approximately  $5^\circ$  in size, in accord with the best resolution expected given our rotational smear. At this stage, we also applied penalty functions designed to minimize surface structure, especially concavities, not needed to fit the observations. These penalties are added to the model  $\chi^2$  to give an objective function; it is this latter value that is minimized during the fit. Also at this stage, we used a higher density grid search (pole spacing of  $\sim 5^\circ$ – $10^\circ$ ) in and around the most promising spin-pole regions. The choice of a final model is somewhat subjective and is based on low objective function residuals and a model's ability to reproduce the subtle features evident in the images without resorting to unrealistic topography. We tend to accept models with muted topography that may have slightly larger residuals over models with lower residuals but less physically plausible topography.

Our best model solutions have  $D_{\text{eff}} = 3.5 \pm 0.4$  km,  $a/b \leq 1.1$ ,  $a/c \leq 1.2$ , and show a preference for spin poles within  $\sim 15^\circ$  of  $\lambda = 317^\circ$ ,  $\beta = -20^\circ$ , indicating retrograde rotation. We investigated prograde rotation at and around the mirror pole ( $\lambda = 137^\circ$ ,  $\beta = +20^\circ$ ), but the  $\chi^2$  residuals are higher and the fits are visually inferior. Our adopted pole is shown in Fig. 10 with a 'P' symbol. Our south pole is  $27^\circ$  from the Sun which is consistent with the large thermal component observed in the IR. Size, shape, and spin pole details for our adopted model are given in Table 7. Our model rotation period is 3.2931 h and is within the uncertainty quoted by Pravec et al. (2006) (Table 1). Fig. 11 shows our model along with the delay-Doppler data and corresponding plane-of-sky view. Fig. 12 shows principal axes views. Regions where the radar incidence angle was



(a)



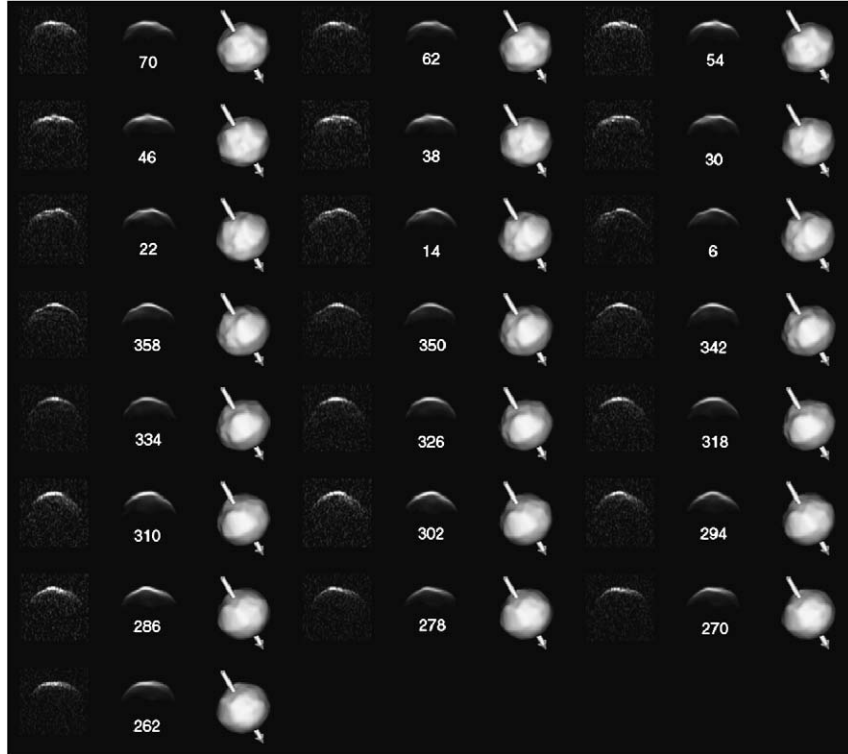
(b)

Fig. 11. Composite of images showing our best model; data (left), modeled data (center, with subradar longitude indicated), and plane-of-sky (POS) view of the model. See Table 7 for properties of this model. (a) 27 August, (b) 30 August, (c) 31 August, (d) 2 September. Resolution has been scaled to 75 m per pixel on all images. Each image frame is 6100 by 6100 m. Images increase in time from left to right, top to bottom (i.e., subradar longitude decreases with time).

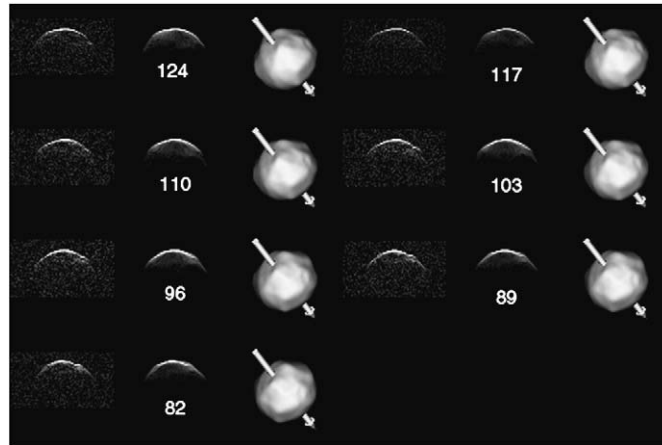
greater than  $60^\circ$  and the terrain was effectively hidden from view are colored yellow. In this case, the north polar region is hidden. Figs. 13 and 14 show our to the CW data and the Pravec et al. lightcurve.

Our primary size estimate makes 2002 CE26 one of the largest NEA binaries observed to date (Pravec et al., 2006). The secondary to primary size ratio is  $\sim 0.09$ , the second smallest observed for an NEA after 1862 Apollo (Ostro et al., 2005b). Our size constraints lead to a visual albedo [Eq. (1)] for the

primary of  $p_v = 0.07 + 0.05/-0.2$  which is consistent with a C-class taxonomy and our thermal model. Using the nominal OC radar cross-section, we estimate 2002 CE26's radar albedo to be  $\hat{\sigma}_{oc} = 0.24 + 0.06/-0.05$ . Typical C-class asteroids among main-belt targets have a mean radar albedo  $\hat{\sigma}_{oc} = 0.15 \pm 0.05$  (Magri et al., 1999). Among NEAs, C-class asteroids have radar albedos comparable to other NEAs (primarily S) with a mean of  $0.16 \pm 0.08$  (Benner, 2006). Our radar albedo is therefore high for a typical C-asteroid, which may



(c)



(d)

Fig. 11. (continued)

indicate a less porous surface regolith than typically found on NEAs.

#### 2.2.4. Secondary orbit

With a shape model to locate a precise primary center-of-mass (COM), we explored further refinements to the secondary orbit as described in Margot et al. (2002). Our best orbit fits (reduced  $\chi^2 < 0.5$ ) have a period  $P = 15.6 \pm 0.1$  h, eccentricity  $e = 0.00 \pm 0.02$ , semi-major axis  $a = 4.7 \pm 0.2$  km, and a range of possible poles as illustrated in Fig. 10 (Table 5). Our semi-major axis is 2.7 primary radii, consistent with most observed NEA binaries (Margot et al., 2002; Pravec et al., 2006). Some of our orbital poles overlap our estimated primary spin pole, consistent with an equatorial orbit. If the

secondary spin pole is parallel to the primary spin pole and the orbit is equatorial, the aspect angle ( $\sim 45^\circ$  on 2 September) and secondary bandwidth result in a secondary rotation period of  $15 + 11/-7$  h, consistent with synchronous rotation.

#### 2.2.5. Primary mass and density

Based on our estimates of the secondary orbit, the mass of the system is  $M = 1.95 \pm 0.25 \times 10^{13}$  kg. Since the secondary is so much smaller than the primary (diameter ratio  $\sim 12$  and volume ratio  $\sim 1700$ ), then for similar bulk densities this is effectively the mass of the primary. Given our primary size estimate, we estimate its bulk density to be  $\rho = 0.9 + 0.5/-0.4$  g cm $^{-3}$ , lower than any other reported main-belt or near-Earth aster-

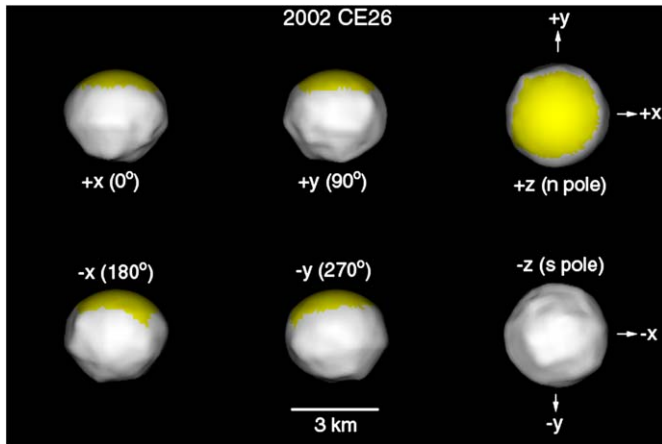


Fig. 12. Principal axis views of our adopted model (Table 7). Major axes and equivalent longitudes are indicated and point out of the image toward the viewer. The yellow color indicates regions where the radar incidence angles were  $>60^\circ$  and are effectively hidden from view.

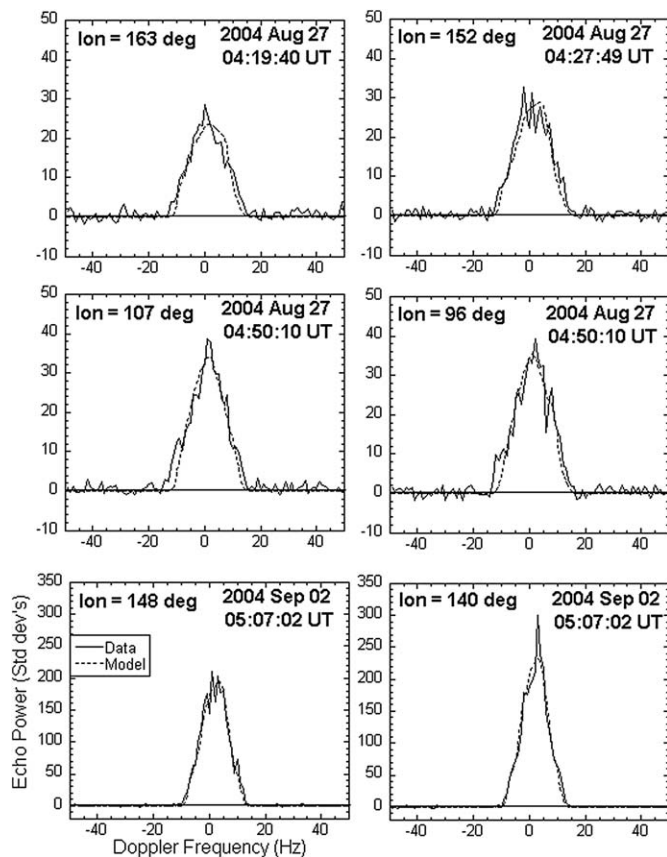


Fig. 13. Model fit (dashed line) to CW data (solid line).

oid (Britt et al., 2002), and comparable to the recent estimate of  $0.8 + 0.2/-0.1 \text{ g cm}^{-3}$  for the Trojan binary 617 Patroclus (Marchis et al., 2006).

Fig. 15 illustrates how our bulk density estimates depend on the primary's diameter. For comparison, we show the range of bulk densities estimated for comets (discussed in Section 3) and the range of bulk densities expected from anhydrous carbonaceous chondrites (CO, CV) for typical grain densities (Britt et al., 2002) and for porosities of  $50 \pm 20\%$ . Note that these es-

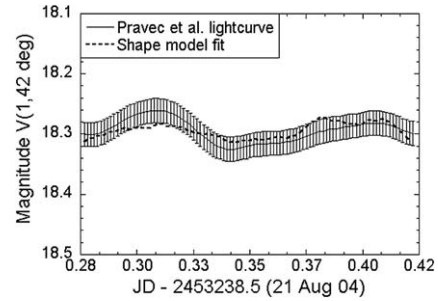


Fig. 14. Model fit (dashed line) to lightcurve of Pravec et al. (2006). Uncertainties shown for lightcurve are based on an RMS residual of 0.02 for the photometric data. Uncertainties on the model fit are comparable in scale but are not shown for clarity.

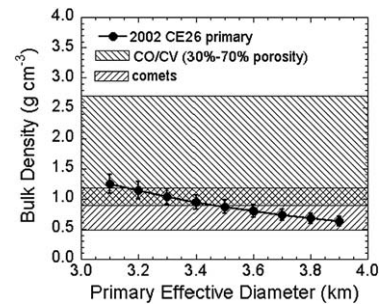


Fig. 15. 2002 CE26 bulk density derived from secondary orbital parameters plotted as a function of the primary diameter. Also shown are estimated bulk densities of anhydrous carbonaceous chondrites (CO/CV) assuming a porosity of  $50 \pm 20\%$  and grain densities of  $3.1\text{--}3.8 \text{ g cm}^{-3}$  (Britt and Consolmagno, 2000) and the range of estimated bulk densities for known comets (Weissman et al., 2004).

timates overlap at bulk densities of  $0.9\text{--}1.2 \text{ g cm}^{-3}$ . If 2002 CE26 is composed of CO/CV chondritic material, its bulk density requires porosities of at least 55% and strongly suggests a “rubble pile” structure. Alternatively, its bulk density is comparable to those estimated for comets and is therefore consistent with more moderate porosities if composed largely of water ice.

### 3. Discussion

What is the origin of this binary system? The most widely accepted mechanism for the formation of NEA binaries is spin-up, tidal distortion, and mass shedding due to close approaches with a terrestrial planet (Bottke and Melosh, 1996; Richardson et al., 1998, 2002; Walsh and Richardson, 2006). 2002 CE26 fits the criteria expected for this mechanism: its shape and bulk density suggest a spheroidal rubble pile; its rotation period is essentially at the spin limit for a spherical strengthless object ( $P_{\text{crit}} \sim 3.5 \text{ h}$  for  $\rho = 0.9 \text{ g cm}^{-3}$ ); and the secondary's orbit appears to be equatorial.

Another candidate mechanism for spinning small asteroids to create binaries is the Yarkovsky–O'Keefe–Radzievskii–Paddack (YORP) effect (Rubincam, 2000). The YORP effect results when surface irregularities absorb and re-emit photons in anisotropic directions, resulting in a net torque that can spin-

up or slow down a small asteroid (<20 km) on timescales of  $10^5$ – $10^6$  yr. Additional options for binary formation include the Smashed Target Satellites (SMATS) and Escaping Ejected Binaries (EEBs) collisional mechanisms described by Durda et al. (2004). Either of these mechanisms could result in a binary being ejected into one of the main-belt resonances and from there perturbed into a near-Earth orbit.

Could 2002 CE26 be an extinct comet? Comets have an estimated bulk density range of 0.5 to 1.2 g cm<sup>-3</sup> (Weissman et al., 2004; Fig. 15). Its optical albedo falls within the 0.04 ± 0.04 range of known comets and suspected extinct comets (Fernandez et al., 2001). Its Tisserand parameter is  $T = 3.065$ , slightly higher than the boundary value of 3 which separates most Jupiter-family comets (JFCs) from the NEA population [for comparison 107P/(4015) Wilson–Harrington has  $T = 3.084$ ] (Weissman et al., 2002; Fernandez et al., 2001). Active comets have low estimated radar albedos ( $0.06 \pm 0.03$ ; Harmon et al., 2004), but there have been no radar detections of known extinct comets. We speculate that an extinct comet might exhibit a higher radar albedo as a consequence of volatile depletion and surface deposition of lag material while retaining a porous, low density interior. Although our IR spectrum shows no evidence of hydrated minerals at 3 μm (e.g., phyllosilicates), even active comets often do not show this feature. A numerical integration (excluding nongravitational forces and terrestrial planetary encounters) shows the most likely source region for 2002 CE26 to be the 3:1 resonance with Jupiter (64% probability) or ν6 secular resonance (23% probability), but not the JFC population (Bottke et al., 2002; W. Bottke, personal communication). Recent work by Levison et al. (2006) suggests encounters with the terrestrial planets could push an extinct JFC into the 3:1 mean-motion or ν6 secular resonance, leading to a more NEA-like orbit; we speculate that this or subsequent encounters might also spin-up an extinct comet and create a binary.

Once a binary is formed, the system is subjected to the binary YORP (BYORP) mechanism (Bottke et al., 2002; Čuk and Burns, 2005). Numerical studies by Čuk and Burns (2005) suggest that BYORP is capable of circularizing the orbit and despinning the secondary to synchronization in  $10^4$ – $10^5$  yr, orders of magnitude more quickly than tidal dissipation. This, however, poses a problem by predicting that binary orbits will rapidly degenerate, leading to either a collision or separation of the components, which is generally inconsistent with the observed number of binary asteroids. To solve this apparent contradiction, Čuk and Burns (2005) suggest that many binary systems are in one of several possible stable states in which the total radiative force becomes zero. The only one of these states that we can test requires a secondary in an equatorial orbit, a semi-major axis of several primary radii, and a primary obliquity (which they define as the angle between the primary equator and the plane of its heliocentric orbit) of 50° to 60° for prograde systems or 120° to 130° for retrograde systems. 2002 CE26's heliocentric orbital pole is  $\lambda = 72^\circ$ ,  $\beta = +42^\circ$  giving an obliquity of 122°. Our results are therefore consistent with this prediction.

#### 4. Future opportunities

The next radar encounter with 2002 CE26 is September 2014 when it will approach to 0.138 AU while within the Arecibo window. Its position will be ~40° away from that in 2004. Predicted peak SNRs at Arecibo are approximately 300 per run (comparable to those on 31 August 2005) and will allow us to refine the shape, size, bulk density, and spin state of the primary, and the orbit of the secondary, and test the hypothesis of a tertiary.

#### Acknowledgments

We thank Ted Howell and Alan Harris (DLR) for their reviews. We thank W. Bottke for locating probable source regions and for helpful discussions and H. Levison for a preprint of his paper. This work was supported by a Bloomsburg University Research and Disciplinary Grant to M.K.S. Student travel for J.S. was supported by Arecibo Observatory. The Arecibo Observatory is part of the National Astronomy and Ionosphere Center, which is operated by Cornell University under a cooperative agreement with the National Science Foundation. Some of this work was performed at the Jet Propulsion Laboratory, California Institute of Technology, under contract with the National Aeronautics and Space Administration. This material is based in part upon work supported by the National Aeronautics and Space Administration (NASA) under the Science Mission Directorate Research and Analysis Programs. Part of the data utilized in this publication were obtained and made available by the MIT-UH-IRTF Joint Campaign for NEO Reconnaissance. The IRTF is operated by the University of Hawaii under Cooperative Agreement No. NCC 5-538 with the National Aeronautics and Space Administration, Office of Space Science, Planetary Astronomy Program.

#### References

- Benner, L.A.M., 2006. Summaries of asteroid radar properties. Available online at [http://echo.jpl.nasa.gov/~lance/asteroid\\_radar\\_properties.html](http://echo.jpl.nasa.gov/~lance/asteroid_radar_properties.html).
- Britt, D.T., Consolmagno, G.J., 2000. The porosity of dark meteorites and the structure of low-albedo asteroids. *Icarus* 146, 213–219.
- Britt, D.T., Yeomans, D., Housen, K., Consolmagno, G., 2002. Asteroid density, porosity, and structure. In: Bottke Jr., W.F., Cellino, A., Paolicchi, P., Binzel, R.P. (Eds.), *Asteroids*, vol. III. Univ. of Arizona Press, Tucson, AZ, pp. 485–500.
- Bottke, W.F., Melosh, H.J., 1996. The formation of asteroid satellites and doublet craters by planetary tidal forces. *Icarus* 124, 372–391.
- Bottke, W.F., Morbidelli, A., Jedicke, R., Petit, J.M., Levison, H.F., Michel, P., Metcalfe, T.S., 2002. Debaised orbital and absolute magnitude distribution of near-Earth objects. *Icarus* 156, 399–433.
- Busch, M.W., Ostro, S.J., Benner, L.A.M., Giorgini, J.D., Jurgens, R.F., Rose, R., Magri, C., Pravec, P., Scheeres, D.J., Broschart, S.B., 2006. Radar and optical observations and physical modeling of near-Earth Asteroid 10115 (1992 SK). *Icarus* 181, 145–155.
- Čuk, M., Burns, J.A., 2005. Effects of thermal radiation on the dynamics of binary NEAs. *Icarus* 176, 418–431.
- Cushing, M.C., Vacca, W.D., Rayner, J.T., 2004. SpeXtool: A spectral extraction package for SpeX, a 0.8–5.5 micron cross-dispersed spectrograph. *Publ. Astron. Soc. Pacific* 116, 362–376.
- Durda, D.D., Bottke, W.F., Enke, B.L., Merline, W.J., Asphaug, E., Richardson, D.C., Leinhardt, Z.M., 2004. The formation of asteroid satellites in large impacts: Results from numerical simulations. *Icarus* 170, 243–257.

- Fernandez, Y.R., Jewit, D.C., Sheppard, S.S., 2001. Low albedos among extinct comet candidates. *Astron. J.* 553, 197–200.
- Fowler, J.W., Chillemi, J.R., 1992. IRAS asteroid data processing. In: Tedesco, E.F. (Ed.), *IRAS Minor Planet Survey*. Technical report PL-TR-92-2049. Phillips Laboratory, Hanscom Air Force Base, Massachusetts, pp. 17–43.
- Harmon, J.K., Nolan, M.C., Ostro, S.J., 2004. Radar studies of cometary nuclei and grain coma. In: Festou, M.C., Keller, H.U., Weaver, H.A. (Eds.), *Comets*, vol. II. Univ. of Arizona Press, Tucson, AZ, pp. 265–280.
- Harris, A.W., 1998. A thermal model for near-Earth asteroids. *Icarus* 131, 291–301.
- Harris, A.W., Lagerros, J.S., 2002. Asteroids in the thermal infrared. In: Bottke Jr., W.F., Cellino, A., Paolicchi, P., Binzel, R.P. (Eds.), *Asteroids*, vol. III. Univ. of Arizona Press, Tucson, AZ, pp. 205–218.
- Hudson, S., 1993. Three-dimensional reconstruction of asteroids from radar observations. *Remote Sens. Rev.* 8, 195–203.
- Levison, H.F., Terrell, D., Weigert, P.A., Dones, L., Duncan, M.J., 2006. On the origin of the unusual orbit of Comet 2P/Encke. *Icarus* 182, 161–168.
- Lord, S., 1992. A new software tool for computing Earth's atmospheric transmission of near- and far-infrared radiation. NASA Technical Memorandum 103957.
- Magri, C., Ostro, S.J., Rosema, K.D., Thomas, M.L., Mitchell, D.L., Campbell, D.B., Chandler, J.F., Shapiro, I.I., Giorgini, J.D., Yeomans, D.K., 1999. Mainbelt asteroids: Results of Arecibo and Goldstone radar observations of 37 objects during 1980–1995. *Icarus* 140, 379–407.
- Mahapatra, P.R., Ostro, S.J., Benner, L.A.M., Rosema, K.D., Jurgens, R.F., Winkler, R., Rose, R., Giorgini, J.D., Yeomans, D.K., Slade, M.A., 1999. Recent radar observations of Asteroid 1566 Icarus. *Planet. Space Sci.* 47, 987–995.
- Marchis, F., Hestroffer, D.C., and 16 colleagues, 2006. A low density of  $0.8 \text{ g cm}^{-3}$  for the Trojan binary Asteroid 617 Patroclus. *Nature* 439, 565–567.
- Margot, J.L., Nolan, M.C., Benner, L.A.M., Ostro, S.J., Jurgens, R.F., Giorgini, J.D., Slade, M.A., Campbell, D.B., 2002. Binary asteroids in the near-Earth object population. *Science* 296, 1445–1448.
- Mitchell, D.L., Ostro, S.J., Hudson, R.S., Rosema, K.D., Campbell, D.B., Velez, R., Chandler, J.F., Shapiro, I.I., Giorgini, J.D., Yeomans, D.K., 1996. Radar observations of Asteroids 1 Ceres, 2 Pallas, and 4 Vesta. *Icarus* 124, 113–133.
- Ostro, S.J., Hudson, R.S., Nolan, M.C., Margot, J.L., Scheeres, D.J., Campbell, D.B., Magri, C., Giorgini, J.D., Yeomans, D.K., 2000. Radar observations of Asteroid 216 Kleopatra. *Science* 288, 836–839.
- Ostro, S.J., Hudson, R.S., Benner, L.A.M., Giorgini, J.D., Magri, C., Margot, J.L., Nolan, M.C., 2002. Asteroid radar astronomy. In: Bottke Jr., W.F., Cellino, A., Paolicchi, P., Binzel, R.P. (Eds.), *Asteroids*, vol. III. Univ. of Arizona Press, Tucson, AZ, pp. 255–271.
- Ostro, S.J., Benner, L.A.M., Nolan, M.C., Magri, C., Giorgini, J.D., Scheeres, D.J., Broschart, S.B., Kaasalainen, M., Vokrouhlicky, D., Chesley, S.R., Margot, J.L., Jurgens, R.F., Rose, R., Yeomans, D.K., Suzuki, S., DeJong, E.M., 2005a. Radar observations of Asteroid 25143 Itokawa (1998 SF36). *Meteorit. Planet. Sci.* 39, 407–424.
- Ostro, S.J., Benner, L.A.M., Giorgini, J.D., Nolan, M.C., Hine, A.A., Howell, E.S., Margot, J.L., Magri, C., Shepard, M.K., 2005b. (1862) APOLLO. *IAU Circ.* 8627.
- Pravec, P., and 55 colleagues, 2006. Photometric survey of binary near-Earth asteroids. *Icarus* 181, 63–93.
- Rayner, J.T., Toomey, D., Onaka, P., Denault, A., Stahlberger, W., Vacca, W., Cushing, M., 2003. SpeX: A medium-resolution 0.8–5.5 micron spectrograph and imager for the NASA Infrared Telescope Facility. *Publ. Astron. Soc. Pacific* 115 (805), 362–382.
- Richardson, D.C., Bottke, W.F., Love, S.G., 1998. Tidal distortion and disruption of Earth-crossing asteroids. *Icarus* 134, 47–76.
- Richardson, D.C., Leinhardt, Z.M., Melosh, H.J., Bottke, W.F., Asphaug, E., 2002. Gravitational aggregates: Evidence and evolution. In: Bottke Jr., W.F., Cellino, A., Paolicchi, P., Binzel, R.P. (Eds.), *Asteroids*, vol. III. Univ. of Arizona Press, Tucson, AZ, pp. 501–516.
- Rivkin, A.S., Binzel, R.P., Bus, S.J., 2005. Constraining near-Earth object albedos using near-infrared spectroscopy. *Icarus* 175, 175–180.
- Rubincam, D.P., 2000. Radiative spin-up and spin-down of small asteroids. *Icarus* 148, 2–11.
- Shepard, M.K., Schlieder, J., Nolan, M.C., Hine, A.A., Benner, L.A.M., Ostro, S.J., Giorgini, J.D., 2004, 2002 CE26. *IAU Circ.* 8397.
- Walsh, K.J., Richardson, D.C., 2006. Binary near-Earth asteroid formation: Rubble pile model of tidal disruptions. *Icarus* 180, 201–216.
- Weissman, P.R., Bottke, W.F., Levison, H.F., 2002. Evolution of comets into asteroids. In: Bottke Jr., W.F., Cellino, A., Paolicchi, P., Binzel, R.P. (Eds.), *Asteroids*, vol. III. Univ. of Arizona Press, Tucson, AZ, pp. 669–686.
- Weissman, P.R., Asphaug, E., Lowry, S.C., 2004. Structure and density of cometary nuclei. In: Festou, M.C., Keller, H.U., Weaver, H.A. (Eds.), *Comets*, vol. II. Univ. of Arizona Press, Tucson, AZ, pp. 501–516.